

Estimating Finite Source Properties of Small Earthquake Ruptures

by Jeffrey J. McGuire

Abstract Many of the most fundamental questions in earthquake science are currently limited by a lack of knowledge about small earthquake ruptures. Small earthquakes are difficult to study owing to the poor constraints placed on many of the interesting physical parameters by bandlimited, far-field, seismic data. Traditionally, dynamic models, such as an expanding circular crack, have been utilized to bridge the gap between the easily measurable quantities for small earthquakes and more interesting physical parameters such as stress drop and rupture velocity. Here I present a method for estimating the basic finite source properties of a rupture that is independent of any *a priori* model and utilizes the description of a finite source, the second moments, that far-field waves are inherently sensitive to. Application to two magnitude 5 events in southern California demonstrates the ability of an empirical Green's function approach to estimating the second moments to resolve the fault-plane ambiguity, rupture length, and overall directivity. Additional results are presented for two example M 2.7 events from the creeping section of the San Andreas fault to examine the likely lower bound on event size that can be studied with surface seismometers. The creeping section earthquakes have very similar rupture areas but would be improperly interpreted as significantly different using the traditional methodology. One of these events presents a relatively clear interpretation of the velocity of rupture front propagation, which is about 0.8 of the Rayleigh speed, suggesting little difference in rupture velocity between it and typical large earthquakes.

Introduction

Once an earthquake instability nucleates, the manner in which the rupture propagates across a fault reflects both the initial properties of the fault and the transient stress field produced by the rupture. The dynamical processes that relate the two are often investigated by examining the dependence of various measurable parameters on earthquake size. Many of these scaling relations, such as the observation of approximately constant stress drop over the entire range of earthquake magnitudes (Scholz, 1990), provide the most fundamental constraints available for testing models of the earthquake process. Implicit in this approach is the assumption that the quantity being evaluated as a function of earthquake size has been accurately measured for events that differ by over 10 orders of magnitude in size. For large earthquakes in densely instrumented areas, the kinematical properties of the rupture are regularly imaged in great detail by combining strong ground motion and geodetic data. These finite fault models resolve many physical quantities, such as average stress drop, rupture velocity, and slip rise time, that are utilized in scaling relation studies. The finite fault inversions rely on the complementary nature of near-field, far-field, and geodetic data for breaking the trade-offs between the large number of parameters needed to describe a rupture in detail. For small earthquakes, near-field and geodetic data

are typically unavailable, making the estimation of finite fault models a nonunique problem. For instance, Venkataraman *et al.* (2000) solved for the slip distribution on each of the two nodal planes of an M_w 4.5 Northridge aftershock in the Los Angeles basin using ~ 140 subfaults and were unable to differentiate between the rupture and auxiliary planes of the focal mechanism based solely on the waveform fits. Thus, the imaging of finite source properties of small earthquakes that is necessary for studying earthquake physics cannot typically be done with the same techniques that are utilized for large earthquakes.

The most easily measured quantities for small earthquakes are the seismic moment, M_0 , and the average corner frequency, f_c . The corner frequency reflects the temporal and spatial finiteness of the source and specifies the frequency above which destructive interference starts to have a first-order effect on the amplitude spectrum of the radiated wave field. To convert these quantities to the ones that are used in scaling relations, such as stress drop ($\Delta\sigma$), a physical model is often imposed. Eshelby (1957) and Brune (1970), respectively, introduced the following expressions relating the stress drop for an expanding circular crack with constant rupture velocity to the average corner frequency:

$$\Delta\sigma = \frac{7}{16} M_0 \frac{1}{r^3}, \quad (1)$$

$$r = 2.21\beta/f_c, \quad (2)$$

where r is the radius of the crack and is β the shear-wave velocity. These formulae have been widely used to estimate the stress drop of small earthquakes. Madariaga (1976) extended this relationship to account for the effect of seismic waves leaving the source at different angles to the crack and hence having different sensitivities to the spatial finiteness. While the circular crack is a simple and instructive model, studies of small earthquakes in well-instrumented regions show that they exhibit spatial variability in their slip distributions similar to large earthquakes (Lanza *et al.*, 1999; Ide, 2001). Moreover, Rubin and Gillard (2000) and Rubin (2002) have suggested, based on earthquake aftershock locations, that the rupture areas of small earthquakes on some faults are systematically elongated along strike. For a source that deviates from the expanding circular crack model, the application of equations (1) and (2), particularly when only a few stations are available, can produce a large error in the stress drop estimate. Figures 1 and 2 show two simulated $M \sim 4$ earthquake ruptures with the same slip distribution and hence the same average static stress drop. The unilateral rupture (Fig. 1) produces significantly longer source pulses than the bilateral rupture (Fig. 2). Converting the corner frequency measurements for these two events into a circular rupture area (via equation 2) yields estimates of the rupture radius for the two events that differ by about a factor of 2. Mapping this difference through equation (1) would yield stress drop estimates that differ by a factor of 8 despite the true stress drops being identical. The combination of this modeling error with the measurement error in the corner frequency may be responsible for much of the 1–2 orders of magnitude scatter typically seen in small earthquake stress drop estimates. To improve the estimates of small earthquake source properties that constrain earthquake mechanics, it is necessary to estimate a parameterization of the rupture that is both well determined and can be related to physical parameters such as stress drop without assuming any strong dependence on a particular dynamic model.

Earthquake Representations

Earthquake catalogs typically represent ruptures as point sources specified by either a epicenter or centroid location and time as well as a moment tensor. The centroid location and time are the spatial and temporal mean (first degree moment) of the moment release distribution. The simplest general representation of an earthquake that contains information about rupture extent and directivity is the point-source representation plus the variances, or second degree moments, of the moment-release distribution (Backus and Mulcahy, 1976a,b; Backus, 1977a,b). Under the as-

sumption of a constant moment tensor during rupture, the second moments are defined as

$$\begin{aligned} \boldsymbol{\mu}^{(2,0)} &= \iint \dot{f}(\mathbf{r}, t)(\mathbf{r} - \mathbf{r}_0)(\mathbf{r} - \mathbf{r}_0) dV dt, \\ \mu^{(0,2)} &= \iint \dot{f}(\mathbf{r}, t)(t - t_0)(t - t_0) dV dt, \\ \boldsymbol{\mu}^{(1,1)} &= \iint \dot{f}(\mathbf{r}, t)(\mathbf{r} - \mathbf{r}_0)(t - t_0) dV dt, \end{aligned} \quad (3)$$

where $\dot{f}(\mathbf{r}, t)$ is a scalar function that describes the spatial and temporal distribution of moment release along the fault (see McGuire *et al.*, 2002), \mathbf{r}_0 is the centroid location, t_0 is the centroid time, and the integrals are taken over the entire source volume and earthquake duration (Backus 1977a,b; McGuire *et al.*, 2001). When $\dot{f}(\mathbf{r}, t)$ is integrated over the volume of the source, it is known as the source time function (STF), $\dot{f}(t)$. The second spatial moment, $\boldsymbol{\mu}^{(2,0)}$, is related to the spatial extent of the rupture, the second temporal moment, $\mu^{(0,2)}$, is related to the duration of rupture, and the mixed moment, $\boldsymbol{\mu}^{(1,1)}$, is related to the rupture propagation.

Properties of the Second Moment Representation

Following Backus (1977a,b) and Silver and Jordan (1983), I define the characteristic dimension, $x_c(\hat{\mathbf{n}})$, of the slip distribution in a direction $\hat{\mathbf{n}}$; the characteristic duration τ_c , the characteristic rupture length L_c , the characteristic (or apparent rupture) velocity v_c , and the average velocity of the instantaneous spatial centroid, \mathbf{v}_0 :

$$\begin{aligned} x_c(\hat{\mathbf{n}}) &= 2\sqrt{\hat{\mathbf{n}}^T \boldsymbol{\mu}^{(2,0)} \hat{\mathbf{n}}}, \quad \tau_c = 2\sqrt{\mu^{(0,2)}}, \\ v_c &= L_c/\tau_c, \quad \mathbf{v}_0 = \boldsymbol{\mu}^{(1,1)}/\mu^{(0,2)}, \end{aligned} \quad (4)$$

where L_c is the maximum value of $x_c(\hat{\mathbf{n}})$ (i.e., corresponding to the largest eigenvalue of $\boldsymbol{\mu}^{(2,0)}$). A characteristic rupture width, W_c , can also be estimated using the second largest eigenvalue of $\boldsymbol{\mu}^{(2,0)}$. Owing to the weighted average nature of the second moments, the characteristic dimensions of a rupture are always smaller than its total dimensions, but they provide an estimate of the region that contributed significantly to the moment release.

Where an earthquake lies on the scale ranging from a perfectly symmetric bilateral rupture to a uniform slip unilateral rupture can be quantified by the ratio of the magnitude of \mathbf{v}_0 to v_c . This quantity, termed the “directivity ratio,” ranges from 0 for a perfectly symmetric bilateral rupture to 1 for a uniform slip unilateral rupture. The 1992 Landers earthquake slip distribution determined by Wald and Heaton (1994) has a directivity ratio of about 0.79, confirming its well-known unilateral nature. For Loma Prieta the slip model of Wald *et al.* (1991) had a directivity ratio of about 0.1, confirming its bilateral nature (McGuire *et al.*, 2002).

Estimating the Second Moments of Small Earthquake Slip Distributions

Studying the earthquake source requires removing the effects of propagation between the earthquake and the seis-

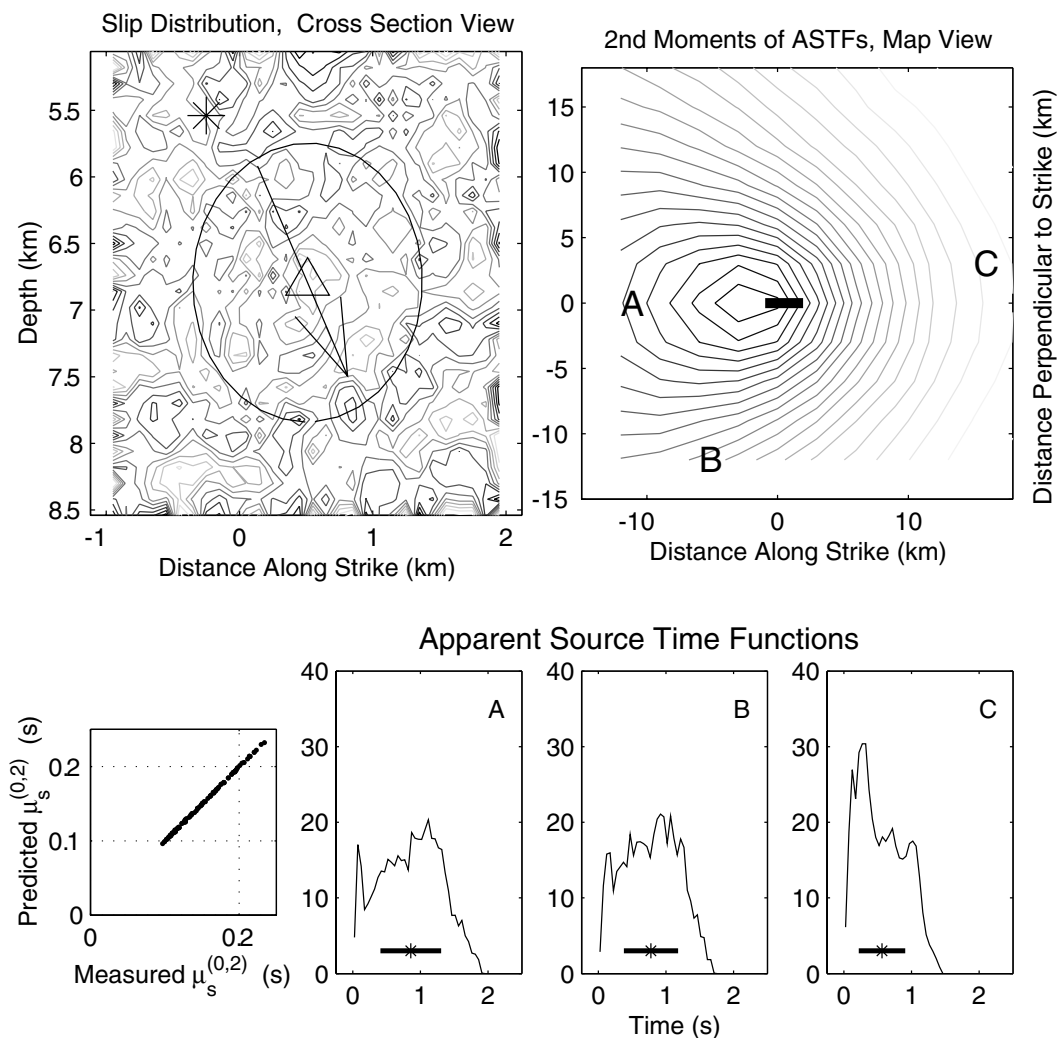


Figure 1. Simulated rupture on a vertical strike-slip fault in an elastic half-space. The top left panel shows the slip distribution on a side view of the fault, with dark-colored contours indicating regions of high slip. The rupture is modeled to begin at the epicenter (asterisk) and spread across the fault with a constant rupture velocity of 3 km/sec and an instantaneous rise time at any particular point. This is a predominately unilateral rupture with a directivity ratio of 0.91. The triangle denotes the centroid of the slip distribution. The ellipse has major and minor axes of length L_c (2.1 km) and W_c (1.7 km), respectively, and is oriented along the eigenvectors of $\mu^{(2,0)}$. The arrow denotes the orientation of $\mu^{(1,1)}$ and is scaled to a length equal to $\tau_c \times v_0$. The upper right panel shows a map view contour plot of the values of $\mu_s^{(0,2)}$ observed at surface stations for P waves, with dark contours indicating large (long) values with a maximum of 0.23 sec and light contours indicating short values with a minimum of 0.09 sec. The bull's eye of dark contours indicates the location where waves that left the source in the direction $-\mu^{(1,1)}$ arrive at the surface. The lower left panel compares the measured value of $\mu_s^{(0,2)}$ with that predicted from the slip distribution's second moments using equation (3). The close agreement between the two indicates that the approximation inherent in equation (3) will produce a much smaller error in estimates of the second moments than measurement error and imprecise knowledge of the slowness vector of the P wave at the source. The lower right panels show ASTFs for three stations whose locations are shown in the map view; the asterisk denotes the apparent centroid time, and the black bar has a length of the apparent τ_c . Stations A and C see relatively long and short ASTFs, respectively, owing to the rupture propagating deeper and in the positive along-strike direction.

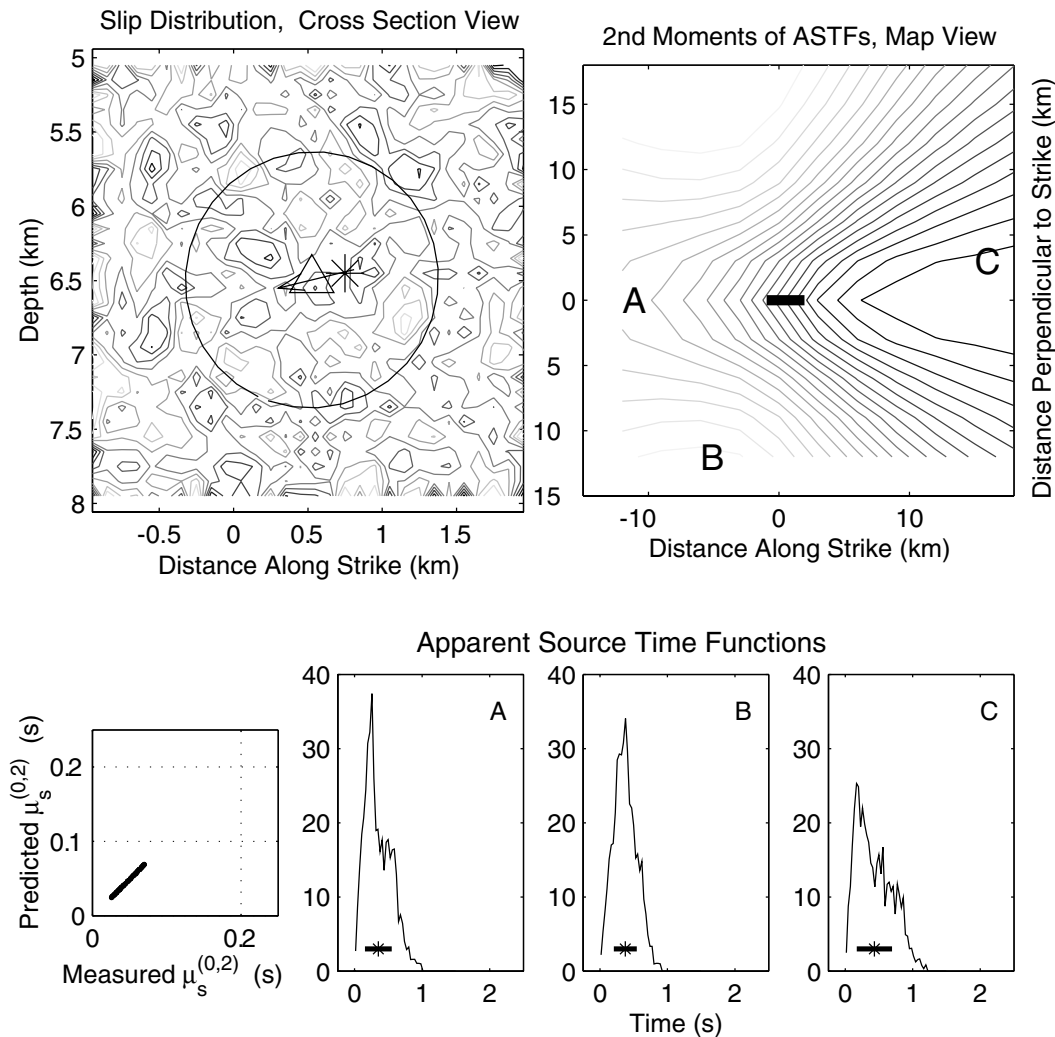


Figure 2. A similar plot to Figure 1, but for a bilateral rupture (epicenter close to centroid). The slip distribution is the same as Figure 1, but the directivity ratio is about 0.1. The true τ_c (average corner frequency) of this slip distribution is approximately a factor of 2 smaller (higher) than for the slip distribution in Figure 1 despite the events having identical seismic moments, rupture areas, and average stress drops.

mic stations. The most accurate approach for small earthquakes is to use the seismograms generated by an even smaller earthquake as an empirical Green's function (EGF) (Hartzell, 1978; Frankel and Kanamori, 1983). The time series that results from the deconvolution of the EGF P (or S) wave from the mainshock P (or S) wave is related to the STF, $\dot{f}(t)$, and is usually referred to as the apparent (or relative) source time function (ASTF). The ASTF is the difference between the STFs of the mainshock and the EGF earthquake as seen from the direction of the observing station through the particular wave type.

Assuming an adequate EGF, the extent to which the ASTF is a distorted image of the STF depends on the spatial extent of the mainshock rupture. The ASTF approximates the STF when the mainshock is effectively a point source in

space compared to the wavelength of the seismic waves being considered. The finite spatial extent of most earthquakes above magnitude 2 produces a systematic variation of the ASTF as a function of take-off angle and wave type in the frequency band recorded by standard short-period seismometers. For a unilateral rupture, the ASTF observed by stations located in the direction of propagation would be significantly shorter in duration than the ASTF observed at stations in the opposite direction (see stations A and C in Fig. 1). For clarity, I term the result from a EGF deconvolution of a P or S wave that left the source region with a slowness vector \mathbf{s} the ASTF, $\dot{f}_s(t)$. For large earthquakes recorded on numerous stations, the inversion of the associated ASTFs for a detailed parameterization of $\dot{f}(\mathbf{r}, t)$ has proven to be a very successful technique for studying rupture propagation (Dreger, 1994).

However, for even moderate earthquakes, the (far-field) ASTFs lack sufficient information to constrain a detailed kinematic source model (Venkataraman *et al.*, 2000).

The effect of spatial finiteness is most easily observed in the general broadening or sharpening of the ASTF at stations located at the most sensitive azimuths. The duration of the ASTF for a phase that leaves the source with a slowness vector \mathbf{s} can be robustly quantified by its variance, $\mu_s^{(0,2)}$, and the associated apparent τ_c ($2\sqrt{\mu_s^{(0,2)}}$). This is an appealing quantity to use for the source extent inverse problem because it is present in many standard source models (Doornbos, 1982). In particular, $\mu_s^{(0,2)}$ is equivalent to the corner frequency in the widely used ω^2 model (Aki, 1967; Brune, 1970; Doornbos, 1982, their equation 11; Silver, 1983, their equation 4).

In practice, EGF deconvolutions often result in an ASTF with a complicated shape. The high-frequency structure of the estimated $f_s(t)$ is often strongly dependent on the regularization of the deconvolution and the choice of the EGF earthquake, making it difficult to evaluate whether this structure results from finite source effects. However, these analyst choices generally produce less than a 10% variability in $\mu_s^{(0,2)}$ for a particular ASTF. Moreover, $\mu_s^{(0,2)}$ should be a smoothly varying function of station position regardless of the details of the moment-release distribution. The map view panels in Figures 1 and 2 show contour plots of $\mu_s^{(0,2)}$ observed at surface stations for the hypothetical slip distribution with two different magnitudes of directivity. These simulations indicate that given a relatively dense station distribution, coherent signals resulting from rupture directivity should be observed in the spatial pattern of $\mu_s^{(0,2)}$ values.

The greatest uncertainty in the measurement of $\mu_s^{(0,2)}$ is in specifying the time interval over which moment release occurred. Many EGF deconvolution algorithms, such as the water-level technique, produce ASTF estimates that have low-amplitude ringing for an extended period of time following the main pulse of moment release that make it difficult to determine the end of the rupture. One technique that provides an objective determination of the duration of $f_s(t)$ is the projected Landweber deconvolution (PLD) algorithm of Betero *et al.* (1997) and Lanza *et al.* (1999). This algorithm performs the deconvolution with moment release restricted to a series of increasing-length time intervals and analyzes the misfit as a function of the interval length (see Fig. 3). The interval length where this trade-off curve flattens out is chosen as the interval during which moment release is allowed (Lanza *et al.*, 1999). This technique produces ASTFs that satisfy a positivity constraint, provide a good fit to the observed seismograms, and are very consistent between nearby stations.

The true second moments are linearly related to $\mu_s^{(0,2)}$ by

$$\mu_s^{(0,2)} \approx \mu^{(0,2)} - 2\mathbf{s} \cdot \boldsymbol{\mu}^{(1,1)} + \mathbf{s}^T \cdot \boldsymbol{\mu}^{(2,0)} \cdot \mathbf{s}, \quad (5)$$

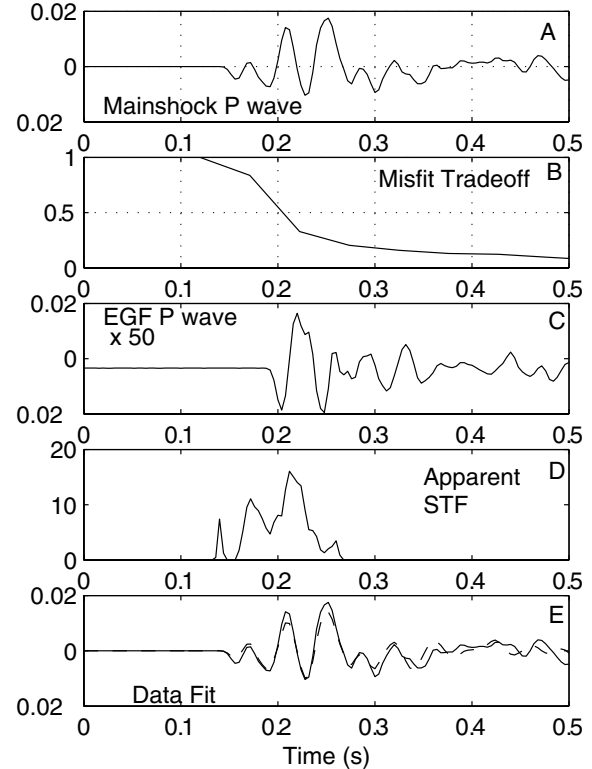


Figure 3. Example of the EGF deconvolution process using the PLD method. (A) The mainshock P wave for an m 2.7 earthquake on the San Andreas fault (see Example Earthquake section) recorded at station AKC (see Fig. 4 for event and station locations). (B) The normalized squared misfit between the observed P wave and the synthetic P -wave resulting from the EGF deconvolution as a function of the time interval during which moment release is allowed to occur where the time coordinate is defined by the P -wave recording in panel A. The value of misfit plotted at a particular time is for the best-fitting STF which has moment release confined to the interval between the origin (i.e., P -wave arrival time) of the event and that time. The misfit curve flattens between about 0.2 and 0.3 sec, indicating that no moment release is required at delays larger than this. (C) The EGF P wave with the scale multiplied by a factor of 50. (D) The ASTF resulting from the deconvolution corresponding to the interval I picked as the inflection point in panel B. (E) The mainshock P wave (solid line) and the synthetic (dashed line) produced by convolving the STF in panel D with the EGF in panel C.

where \mathbf{s} is the slowness vector of the P (or S) wave at the source (i.e., the unit vector along the P [or S] wave take-off direction divided by the wave speed). Equation (3) was first presented in the frequency domain by Doornbos (1982) and then in both the time and frequency domain by Silver (1983). The approximation that results in equation (3) is equivalent to equating the travel time, T , between a point on the fault

(\mathbf{r}) and the station to the zeroth- and first-order terms in the Taylor series expansion about the epicenter, \mathbf{r}_e

$$T = T(\mathbf{r}_e) + \nabla T \cdot (\mathbf{r} - \mathbf{r}_e). \quad (6)$$

This approximation is routinely used to linearize the earthquake location problem and hence, the inverse problem suggested by equation (3) shares many properties with the earthquake location problem. The extent to which the various components of $\mu^{(2,0)}$, $\mu^{(0,2)}$, $\mu^{(1,1)}$ can be uniquely determined is specified by the range of slowness vectors of the various phase–station pairs contained in the data set. For instance, if all of the $\mu_s^{(0,2)}$ measurements are of P waves in the same focal hemisphere, then there will be an unresolved trade-off between rupture duration and rupture propagation toward/away from the stations. This trade-off is analogous to the origin time versus depth trade-off that is inherent in teleseismic earthquake location, and it can be broken in the same way by adding S -wave measurements at the same station set (i.e., observations that have the same partial derivative for $\mu^{(0,2)}$ but different partial derivatives for $\mu^{(1,1)}$ and $\mu^{(2,0)}$) or more effectively by using stations (or phases like pP) corresponding to slowness vectors in the opposite focal hemisphere.

Equation (3) is linear in the 10 unique elements of $\mu^{(2,0)}$, $\mu^{(0,2)}$, and $\mu^{(1,1)}$, suggesting a straightforward inverse problem. However, the 10 elements of the second moments are not independent owing to the physical constraint that the four-dimensional source region have nonnegative volume. This constraint is equivalent to requiring the four by four matrix

$$\begin{bmatrix} \mu^{(0,2)} & \mu^{(1,1)T} \\ \mu^{(1,1)} & \mu^{(2,0)} \end{bmatrix}$$

to be nonnegative definite (McGuire *et al.*, 2001), and it can be enforced using the semidefinite programming algorithm of Vandenberghe and Boyd (1996). If only a few stations are available and the earthquake is clearly associated with a major fault, then the second moments can be constrained to be planar with the strike and dip of the known fault plane, reducing the number of unknown parameters to six. By enforcing these constraints, the dimension of the model space is further limited, making this the most well-posed inverse problem possible for the finite source properties of small earthquakes. Despite this minimal parameterization, the second moment representation is a general one (i.e., every slip distribution has second moments). Thus, the inverse problem described in this section does not impose any *a priori* model on an earthquake and requires resolution of the minimum number of parameters necessary for a description of the earthquake source that includes information about its finite extent.

Many other well-known properties of seismic source inversion are evident in equation (3). When the earthquake is a spatial point source, the elements of $\mu^{(2,0)}$ and $\mu^{(1,1)}$ are

identically zero and the variance of the ASTF is equal to the variance of the true STF. Owing to the positive definite property of $\mu^{(2,0)}$, the finite spatial extent of an earthquake can only make its duration appear longer than the true duration (i.e., the third term on the right-hand side is always positive). The effect of rupture propagation is dependent on the cosine of the angle between the average propagation direction ($\mu^{(1,1)}$) and the take-off angle \mathbf{s} . This second term can be positive or negative (i.e., the rupture appears longer or shorter than it is) depending on whether the rupture is propagating away from or toward the station (in a take-off angle sense). This dependence is widely used in directivity studies and was first derived for surface-wave amplitude spectra radiated from a unilateral rupture model by Ben-Menahem (1961) (see also Boatwright, 1980). However, equation (3) is valid for any kinematic source geometry. Finally, for a given earthquake–station pair, S waves are more sensitive to directivity than P waves owing to their slower wave speeds (i.e., they have a larger magnitude \mathbf{s}).

Example Earthquakes

Southern California

To demonstrate the effectiveness of the EGF-based algorithm for estimating the second moments, we first present two example earthquakes from southern California, the 2002 Yorba Linda earthquake and the 2001 Big Bear City earthquake. For large earthquakes, it is possible to ground truth second moment estimation techniques with estimates of the source distribution derived from near-field seismic and/or geodetic data. While this approach cannot be applied quantitatively to small earthquakes, we present these two cases because their aftershock distributions and strong ground motion distributions allow us to qualitatively evaluate the ability of the second moments to identify the rupture and auxiliary planes and resolve the rupture length and directivity.

The 9 September 2002 M 4.8 Yorba Linda earthquake's hypocenter was located at 13 km depth, just northeast of the Whittier fault in the Los Angeles basin (Fig. 4). The event's focal mechanism showed either right-lateral strike-slip motion on a plane roughly coincident with the Whittier fault or left-lateral motion on the conjugate northeast–southwest-oriented plane. In the absence of other information, it would have been natural to ascribe this event to rupture of the Whittier fault, but its aftershock distribution was elongated in the northeast–southwest orientation with a length of about 3 km, suggesting the conjugate fault plane had actually ruptured (Fig. 4). Additionally, contours of peak ground acceleration (PGA) determined through the U.S. Geological Survey (USGS) shakemap procedure were elongated to the northeast. The shakemap cannot be used unambiguously to identify the rupture plane and directivity because it reflects both source directivity and local site effects. However, several smaller events (5 January 1998, 7 December 1999, 6 March 2000, 13 April 2001) located within a few kilometers of the Yorba

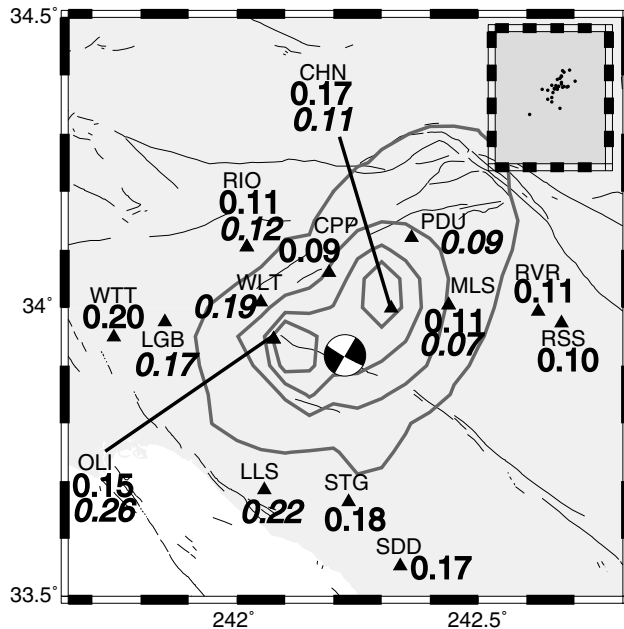


Figure 4. Map of the Yorba Linda earthquake source region (focal mechanism). Stations are labeled with the apparent characteristic durations ($2\sqrt{\mu_s^{(0,2)}}$) in seconds, observed for *P* and *SH* (italic) waves. Relatively short ASTFs were observed to the northeast and relatively long ones to the southwest. The contours denote regions of high PGA from the USGS shakemap procedure. The inset shows a blowup of the aftershock distribution which is elongated in the northeast–southwest direction. Gray lines denote active faults.

Linda earthquake have PGA contours that form concentric circles around the epicenter, suggesting that the pattern seen in Yorba Linda likely resulted from source directivity toward the northeast.

I used the second moment estimation technique to verify that the northeast–southwest nodal plane was indeed the rupture plane of the Yorba Linda Earthquake. An *M* 2.9 aftershock (ID 9818441) was used as the EGF owing to its good signal-to-noise ratio and difference of about a factor of about 90 in seismic moment (integral of the ASTFs). *P* and *SH* seismograms (100 samples per second, HH component) were bandpass filtered between 0.5 and 10 Hz for both the EGF and the mainshock prior to applying the PLD algorithm. Figure 5 shows examples of the EGF deconvolution results. At stations to the northwest, the mainshock and EGF seismograms have relatively similar pulse widths for the main (*P* or *S*) arrival, while at stations to the southwest, the mainshock arrivals are significantly longer than the EGF events. Consequently, the resulting estimates of $\mu_s^{(0,2)}$ showed relatively short values at stations to the northeast and relatively long values at stations to the southwest. Inversions of the $\mu_s^{(0,2)}$ values (Fig. 4; Table 1) were calculated assuming each of the nodal planes was the rupture plane. To evaluate which plane provided a better fit, we used a slightly modified ver-

sion of the variance reduction. Because the coefficient that multiplies $\mu^{(0,2)}$ in equation (3) is the same for all stations, the mean value of the data is easily fit for either fault plane. Thus, a more appropriate measure of the fit is to calculate the variance reduction of the data with its mean removed. These modified variance reductions were 23% and 75% for the northwest- and northeast-striking planes, respectively. Thus, we conclude that the rupture occurred on a small conjugate structure normal to the Whittier fault. The second moment estimates (Table 2) for this plane correspond to an L_c of 1.3 km (shallower to the northeast), a W_c of 0.03 km, a τ_c of 0.15 sec and a v_c of 8.2 km/sec, a v_0 of 4.6 km/sec, and a directivity ratio of 0.77 oriented to the northeast and shallower. The northeast directivity is consistent with the shakemap. Additionally, the 1.4-km L_c , which is always shorter than the total rupture length, is roughly consistent with the aftershock distribution. The estimate of v_0 appears larger than would be likely at the source depth of the mainshock, possibly indicating that τ_c is underestimated, and W_c is not well resolved.

The 10 February 2001 *M* 5.1 Big Bear City earthquake's hypocenter was located at 9 km depth, in the region between the San Andreas and Helendale faults (Fig. 6). The event's focal mechanism showed either right-lateral strike-slip motion on a northwest-striking plane subparallel to the San Andreas and Helendale faults or left-lateral motion on the conjugate northeast–southwest–oriented plane. The aftershock distribution was somewhat elongated in the northeast–southwest orientation with a length of about 3 km, suggesting the conjugate fault plane had actually ruptured (Fig. 6). The USGS shakemap procedure found contours of PGA that were roughly concentric circles around the epicenter, indicating a lack of strong directivity.

I used the second moment estimation technique to the Big Bear City earthquake using an *M* 2.9 foreshock (ID 9627073) as the EGF owing to its good signal-to-noise ratio and difference of about a factor of about 600 in seismic moment (integral of the ASTFs) from the mainshock. *P* and *SH* seismograms (100 samples per second, HH component) were bandpass filtered between 0.5 and 10 Hz for both the EGF and the mainshock prior to applying the PLD algorithm. Figure 7 shows examples of the EGF deconvolution results. There is relatively little azimuthal variation in $\mu_s^{(0,2)}$, but stations to the southwest show slightly longer ASTFs than those in other directions. Inversions of the $\mu_s^{(0,2)}$ values (Fig. 6; Table 1) were calculated assuming each of the nodal planes was the rupture plane to evaluate which plane provided a better fit. The modified variance reductions were 22% and 79% for the northwest- and northeast-striking planes, respectively. Thus, we conclude that the rupture occurred on the northeast-striking plane. The second moment estimates (Table 2) for this plane correspond to an L_c of 2.2 km (northeast–southwest), a W_c of 0.3 km, a τ_c of .35 sec and a v_c of 6.4 km/sec, a v_0 of 1.1 km/sec, and a directivity ratio of 0.17 oriented to the northeast and shallower. The nearly bilateral rupture inferred from the second moments is consistent with

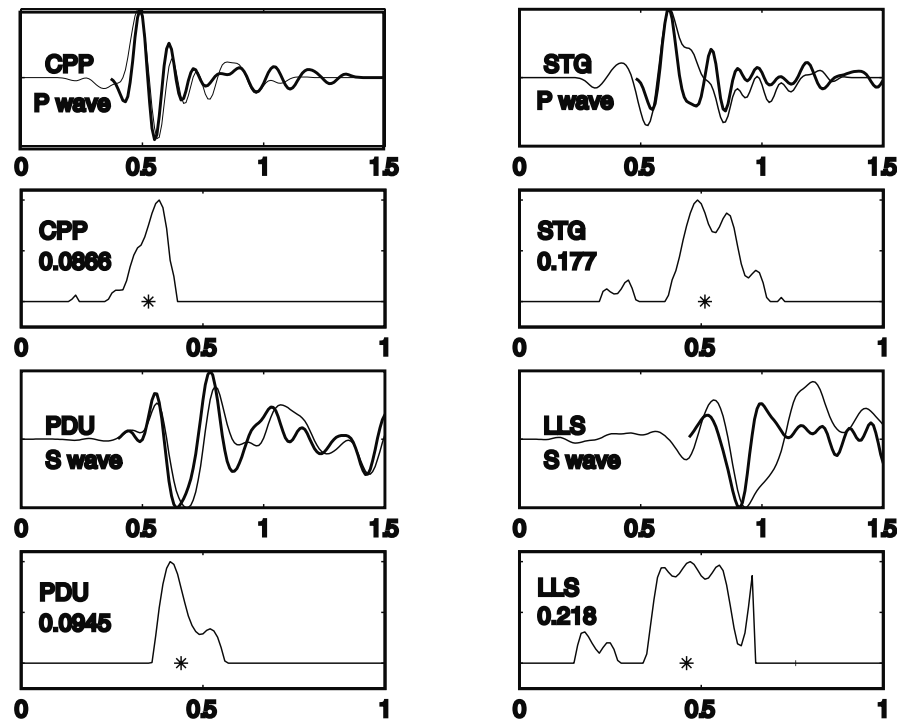


Figure 5. Examples of mainshock (thin) and EGF waveforms (thick) for the Yorba Linda earthquake. For each station, the lower panel shows the ASTF resulting from the PLD estimation procedure, and the asterisk denotes the mean (centroid) time of the ASTF. Each station is labeled with its apparent characteristic duration in seconds.

Table 1
Second Moment Estimates in the Along-Strike (x), Downdip (y), and Time (t) Coordinate System

Event (yyyy mm/dd)	tt (sec ²)	xt (km/sec)	yt (km/sec)	xx (km ²)	xy (km ²)	yy (km ²)
2002 09/03	0.0058	0.0111	-0.0242	0.0816	-0.1602	0.3162
2001 02/10	0.0298	0.0068	0.032	0.3888	-0.5788	0.9214
1994 12/27	0.00043	0.00024	-0.00052	0.00039	-0.00128	0.00449
1995 04/15	0.00059	0.00121	0.00009	0.00245	0.00024	0.00100

the shakemap, and the 2.2-km L_c is roughly consistent with the aftershock distribution.

San Andreas Creeping Section

The spatial extent of the magnitude 5 earthquakes discussed earlier was sufficiently large to allow their finite source properties to be verified through aftershock locations. However, the most interesting events for studying earthquake scaling relations are small enough to prevent this type of argument. Magnitude ~ 2 earthquakes generally have only a few aftershocks, and those can be multiple-source dimensions away from the mainshock, making it difficult to image the rupture extent of an individual mainshock even with advanced relocation techniques, although this approach appears to be effective for the aggregate of a large population of events (Rubin, 2002). Here, I present estimates of the second moments for two M 2.7 earthquakes located on the Bear Valley region along the northern part of the creeping

section of the San Andreas fault. The 29 December 1994 (03:56:12.9 UTC) and 15 April 1995 (11:43:06.57 UTC) earthquakes occurred 3 km apart at a depth of about 3 km and were assigned magnitudes of 2.74 and 2.76, respectively, by the Northern California Seismic Network (NCSN). Given their proximity and correspondence in magnitude, one might expect these two events to have had similar-sized rupture areas and hence stress drops. Fortunately, they were recorded by a dense temporary array of short-period seismometers (L2's, L4's, and L22's) deployed as part of the Incorporated Research Institutions for Seismology-Program for Array Seismic Studies of the Continental Lithosphere (IRIS-PASSCAL) program by Thurber *et al.* (1997) (Fig. 8). The stations of this array had an unusually high sampling rate of 250 Hz, providing high-quality on-scale recordings particularly at the hard rock sites on the southwest side of the fault. These events were also recorded by the NCSN but most nearby stations clipped owing to the bandwidth of the

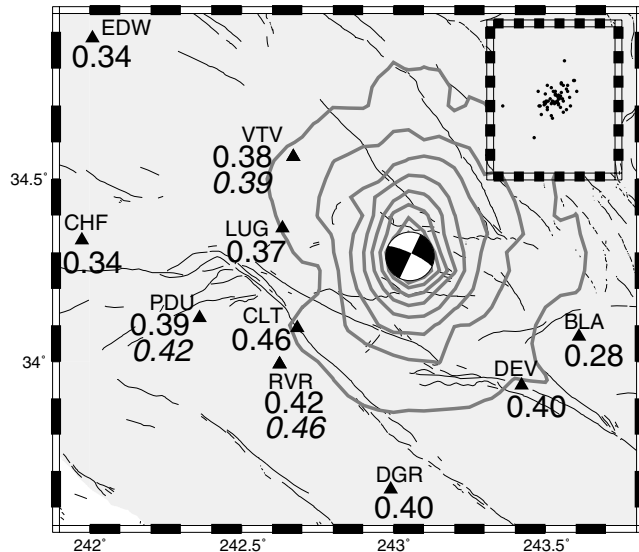


Figure 6. Map of the Big Bear Lake earthquake source region (focal mechanism). Stations are labeled with the apparent characteristic durations ($2\sqrt{\mu_s^{(0,2)}}$) in seconds, observed for *P* and *SH* (italic) waves. The contours denote regions of high PGA from the USGS shakemap procedure. The inset shows a blowup of the aftershock distribution which is elongated in the northeast-southwest direction. Gray lines denote active faults.

telemetry system. One exception is station BSG (Fig. 8), which has a low-gain channel (VLZ) for recording large events. BSG's sample rate, 100 Hz, is not ideal, but by combining EGF recordings on the high gain channel (VHZ) with mainshock recordings on the low gain channel, it yields ASTFs that are consistent with the higher quality records from the temporary stations.

Choice of the EGF. An *M* 1.5 foreshock of the 1994 event and an *M* 0.5 aftershock of the 1995 event were selected as the EGF events based on minimal distance separation from their respective mainshocks and agreement of the first and *SH* waveform polarities with the mainshock. Additionally, we tried to maximize the difference in seismic moment between the EGF and mainshock. Many authors determine the largest event whose duration is still obscured by attenuation by comparing the increase in the duration of the first pulse on velocity seismograms with EGF magnitude (Frankel and Kanamori, 1983; Lanza *et al.*, 1999) and then only use EGFs with magnitudes smaller than the cutoff magnitude. Owing to the very short epicentral distances and the short duration of the deployment, we did not have enough earthquakes with similar ray paths to use this technique. However, multiple EGF events in the magnitude 0.5–1.5 range were tested for each mainshock. To evaluate whether the *M* 1.5 foreshock was too large to use as an EGF for the 1994 event, we compared the ratio between $\mu_s^{(0,2)}$ calculated with the *M* 1.5 EGF

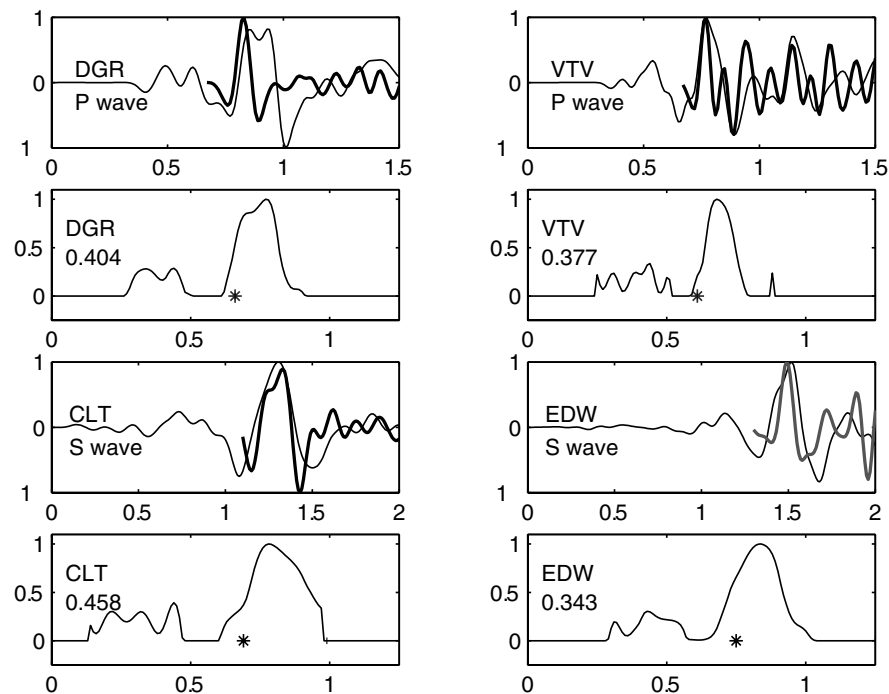


Figure 7. Examples of mainshock (blue) and EGF waveforms (red) for the Big Bear Lake earthquake. For each station, the lower panel shows the ASTF resulting from the PLD estimation procedure, and the asterisk denotes the mean (centroid) time of the ASTF. Each station is labeled with its apparent characteristic duration in seconds.

Table 2
Characteristic Rupture Dimensions Derived from the Second
Moment Estimates in Table 1

Event (yyyy mm/dd)	τ_c (sec)	L_c (km)	W_c (km)	V_0 (km/sec)	L_c/L_0
2002 09/03	0.15	1.3	0.03	4.5	0.77
2001 02/10	0.35	2.2	0.3	1.1	0.17
1994 12/27	0.0413	0.1393	0.0094	1.3	0.40
1995 04/15	0.0488	0.0997	0.0621	2.0	0.99

and that calculated with an M 0.9 EGF at numerous stations. While the ASTFs calculated with these two EGFs differed by a factor of 4 in their moment, roughly as expected, their estimates of $\mu_s^{(0,2)}$ were indistinguishable. If the finite duration of the M 1.5 event was affecting the waveform, cube-root scaling would have predicted the apparent τ_c values to be about 1.6 times larger for the M 0.9 EGF than for the M 1.5 EGF. Instead we found the ratio of these two quantities to be 0.97 ± 0.06 . Given the nearly identical estimates of $\mu_s^{(0,2)}$ produced by the two potential EGFs, we chose to use the M 1.5 EGF, which was large enough to have its waveforms archived by the NCSN data center (the M 0.9 event was not), thus allowing us to also use station BSG. Overall, the choice of EGF event, within reasonable bounds, appears to contribute less than 10% uncertainty in the estimated values of $\mu_s^{(0,2)}$ for most stations. Moreover, since directivity is observed to produce a factor of 4 variation in $\mu_s^{(0,2)}$ (discussed later), any potential errors or biases in $\mu_s^{(0,2)}$ produced by the choice and size of the EGF appear to be significantly smaller than the finite source effects we are seeking to isolate.

The results of the EGF deconvolution for the two M 2.7 mainshocks recorded by the temporary array are shown in Figures 9, 10, 11, and 12. The 1995 event shows a coherent spatial pattern in the estimated $\mu_s^{(0,2)}$ values (Fig. 5; Table 3) with long ASTFs observed at stations located along strike to the northwest and short ASTFs observed at station located at azimuths between east and south (GIB, VLT, BSG). This azimuthal variation is evident in both the comparison of raw mainshock and EGF waveforms as well as the resulting ASTFs (Fig. 10). In contrast, the 1994 event shows generally shorter ASTFs than the 1995 event and much less overall variability in the estimates of $\mu_s^{(0,2)}$ (Fig. 11; Table 4). For many stations, the EGF and mainshock P waveforms are nearly identical in shape (Fig. 12). Figures 10B and 12B show examples of the variation in waveform misfit with increasing $\mu_s^{(0,2)}$ for particular stations. These curves demonstrate that significantly shorter ASTFs than the optimal value determined in the PLD algorithm produce noticeably greater misfit, while significantly longer values are not required by the data. Moreover, they demonstrate that the apparent lengthening/shortening of the ASTFs in the 1995 event is indeed required by the waveforms (for example station VLT versus BRG in Fig. 10B).

The measurements of $\mu_s^{(0,2)}$ in Tables 3 and 4 were inverted for estimates of the second moments using the method

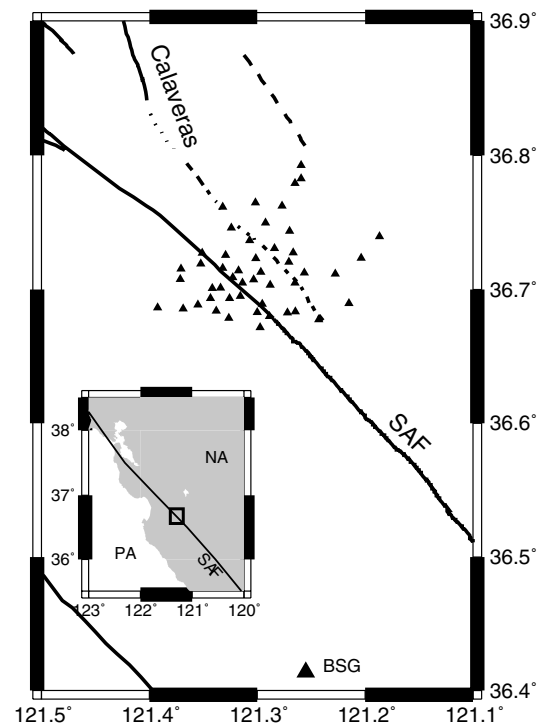


Figure 8. Regional map of the Bear Valley section of the San Andreas fault (SAF). Small triangles show the locations of stations deployed as part of a temporary short-period seismic network by Thurber *et al.* (1997). The large triangle denotes the location of NCSN station BSG that is also used in the directivity studies. Small inset shows the location of the study area (square) in the larger context of the Pacific (PA)–North America (NA) plate boundary.

described in the previous section. Owing to the limited number of stations to the southeast, the source was constrained to be planar with the strike of the San Andreas. The greatest potential sources of bias result from uncertainty in the hypocenter locations and velocity structure. There is a $\sim 25\%$ velocity contrast across this portion of the fault (Stewart, 1968; McNally and McEvilly, 1977; Walter and Mooney, 1982; Thurber *et al.*, 1997). This velocity contrast has produced long-running debates about the dip of the San Andreas and whether the hypocenters are significantly (1–2 km) offset to the southwest of the surface fault trace (Thurber *et al.*, 1997). Thurber *et al.* performed a tomographic inversion using the data from the 6-month-long deployment and some active source experiments. Their results indicate that the San Andreas fault dips approximately 70° to the southwest, causing the epicenters to be a few kilometers offset from the surface trace. For each event, 200 inversions were performed with a random epicenter shift between 0 and 2 km, a random dip between 40° and 90° , and a depth between 2.5 and 4.5 km. Slowness vectors were calculated using 1D raytracing with different velocity models for the two sides of the fault that roughly approximated the tomographic study of Thurber *et al.* (1997). The results of the inversions are shown in

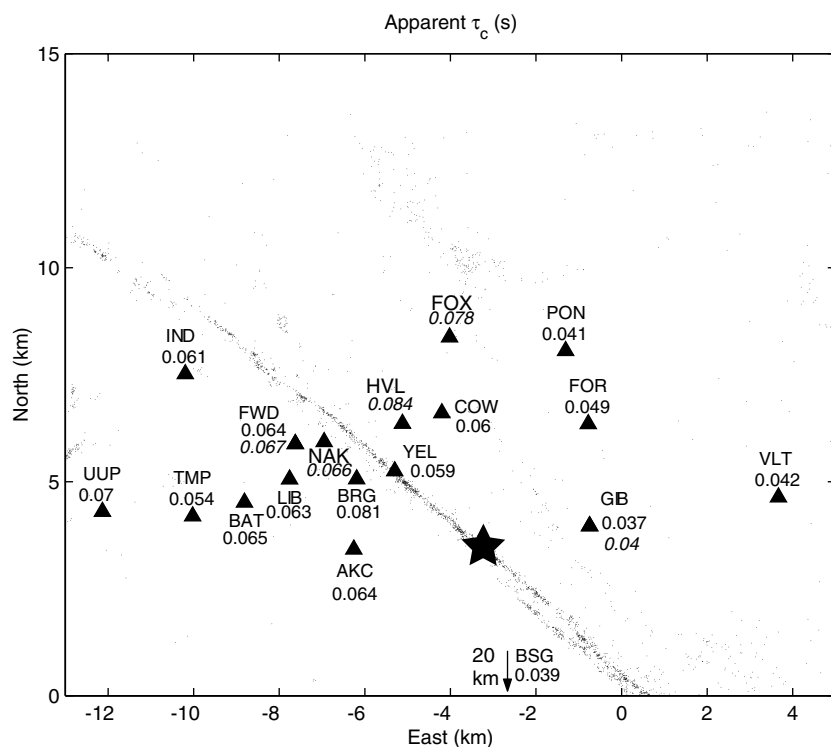


Figure 9. Map of the EGF deconvolution results for a magnitude 2.7 earthquake at 3 km depth on the San Andreas fault on 15 April 1995. Background seismicity, which has been relocated using the relative location technique of Waldhauser and Ellsworth (2000), is shown as small black dots. The mainshock epicenter is denoted by a large black star. Stations of the PASSCAL deployment by Thurber *et al.* (1997) for which EGF measurements were made are shown by black triangles. Each station is labeled with the apparent τ_c values in seconds estimated for it with P -wave values displayed above S -wave values at stations for which both were measured. Station BSG of the NCSN is off the scale of this map (see Fig. 4), but its value and location direction are shown at the bottom of the map. Stations to the northwest along strike have apparent τ_c values that are longer than stations to the southeast owing to the unilateral rupture to the southeast in this event.

Figures 13 and 14. The misfit for both earthquakes was relatively insensitive to the small hypocenter shifts, but for the 1994 event there was a strong preference for fault dips less than about 75° (Fig. 13) in agreement with the tomographic study (Thurber *et al.*, 1997). Tables 3 and 4 present the results for inversions with a dip of 70° and an epicenter shift of $+0.005^\circ$ N and $+0.005^\circ$ E from the double-difference locations. This shift is in the range of minimum misfits and produces locations that match first motion polarities for events in the center of the array.

The characteristic rupture dimensions (Table 2) derived from the second moment estimates indicate that the primary difference between the 1994 and 1995 earthquakes was in their directivity. To evaluate the uncertainty in the characteristic quantities, I plot histograms of their values for the inversions with low misfits in Figure 14. The spread in the histograms is indicative of how much error likely results from uncertainties in the ray paths, the primary source of systematic error. The characteristic rupture lengths, durations, and velocities appear to be fairly robust, but the characteristic rupture widths have spreads of more than 100% of their peak value, indicating a lack of resolution. In particular, the two earthquakes have very similar characteristic rupture lengths and durations. The primary difference between them is that the 1994 event has a value of v_c that is almost twice that of the 1995 event, while the 1995 event has a value of v_0 that is almost twice that of the 1994 event. These differences result from the 1994 event being primarily bilateral, while the 1995 event is primarily unilateral. For a unilateral Haskell rupture, which probably approximates the 1995 event, $v_0 = v_c = v_r$ (the rupture velocity), while for a bi-

lateral rupture with a symmetric slip distribution, a model that may approximate the 1994 event, $v_0 = 0$ and $v_c = 2v_r$. Thus, even though the measurements of $\mu_s^{(0,2)}$ differ by about a factor of 2 in some azimuths, the ruptures had approximately the same rupture length and moment.

Discussion

The example earthquakes presented in the previous section demonstrate that the basic source dimensions are retrievable and the fault-plane ambiguity is resolvable for earthquakes as small as magnitude ~ 2.5 if a sufficient array of standard short-period seismometers is available. Moreover they point out the dangers in using the more standard approaches to stress drop estimation, which would result in a significantly lower estimate of $\Delta\sigma$ for the 1995 creeping section event than the 1994 event, even though the opposite is probably true (the 1994 event had a slightly larger L_c value, and the two events had nearly the same seismic moments). This error results from the assumption of a symmetric circular rupture when there is actually significant directivity present. The ASTFs in Figure 10 also point out the potential dangers in using pulse widths as a measure of directivity. The multiple subevent nature of the 1995 earthquake, at least when viewed from stations to the northwest, could produce a relatively narrow first pulse at these stations simply because it does not result from the entire rupture. Given the relatively minimal amount of effort required to invert equation (3) as compared to the standard corner frequency interpretation schemes (equations 1 and 2), estimat-

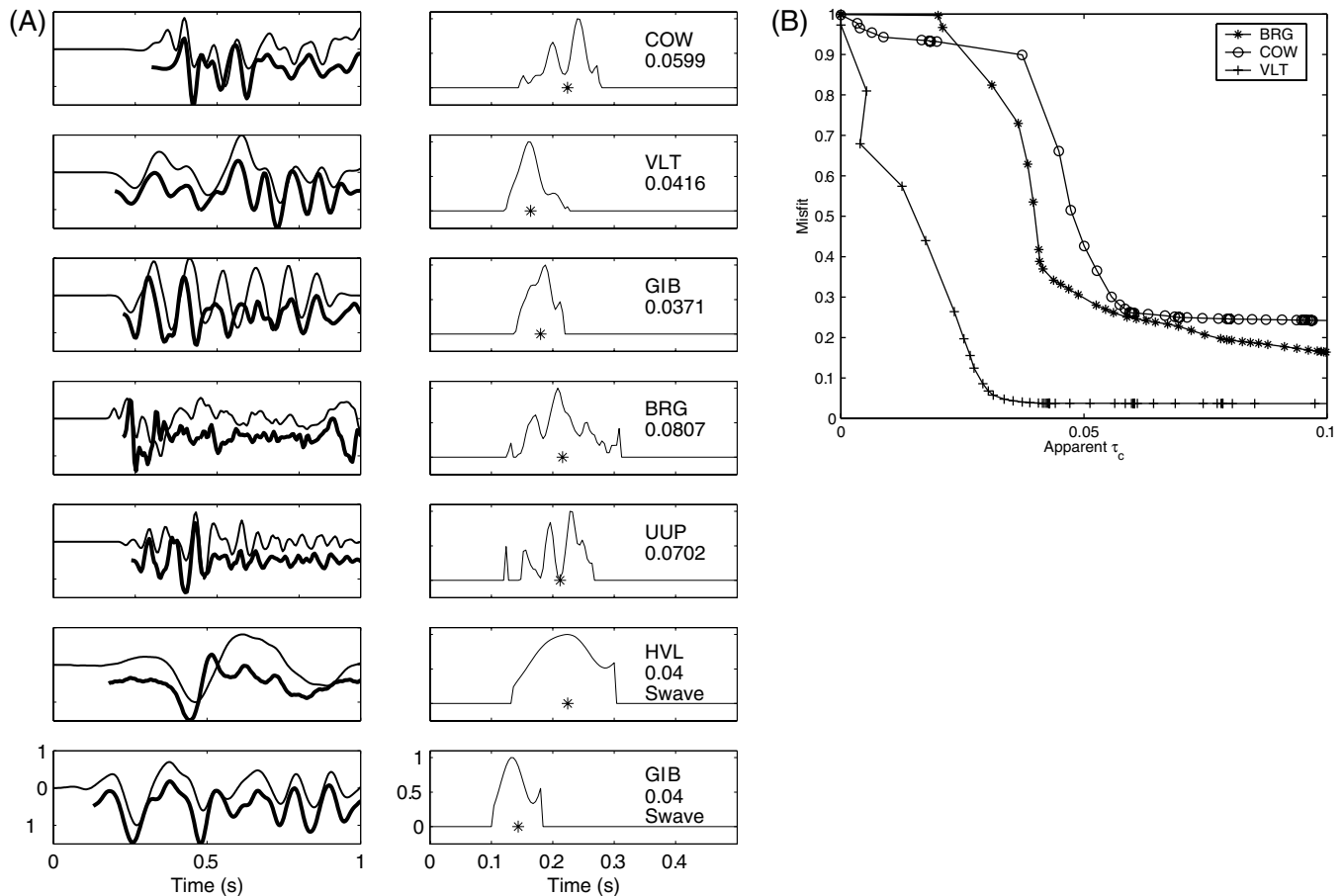


Figure 10. EGF deconvolutions for the 15 April 1995 M 2.7 earthquake on the San Andreas fault. (A) The left-hand panel for each station compares the mainshock (thin) and EGF (thick, offset below the mainshock waveform) P -waveforms. The right-hand panel shows the ASTF resulting from the PLD estimation procedure. All amplitudes have been normalized for plotting purposes. Each ASTF is labeled with the station name (see Fig. 9 for locations) and the apparent τ_c value (see Table 3). (B) Examples of the misfit versus duration trade-off for several stations. The misfit was calculated assuming various length intervals over which the ASTF can be nonzero. The comparison of the resulting ASTF variances (apparent τ_c) with misfit allows a visual assessment of how well constrained the apparent τ_c estimates are.

ing the second moments is a preferable way to analyze small earthquakes.

Resolving the Fault-Plane Ambiguity

The second moments provide additional uses beyond comparing seismic moment and rupture area (i.e., evaluating stress drop), including resolution of the fault-plane ambiguity. For a planar source, $x_c(\hat{n})$ will be identically zero in the direction normal to the fault plane, providing a natural test for discriminating between the two candidate nodal planes of an event's focal mechanism. We did not attempt to invert for the full three spatial dimension representation of the second moments; instead we performed two inversions, one assuming each plane was the rupture plane, for

the southern California events and compared the variance reductions. For each event, the plane with significantly higher variance reduction was confirmed to be the true rupture plane by the aftershock distribution. Moreover the variance reductions achieved when incorrectly assuming the conjugate plane was the true rupture plane were quite small ($\sim 25\%$), indicating that this approach is unlikely to produce a misidentification of the rupture plane owing to the minimal parameterization of $\dot{f}(\mathbf{r}, t)$. Small to moderate earthquake focal mechanisms are one of the most useful data sets for determining the spatial and temporal variation in the crustal stress field (Hardebeck and Hauksson, 2001). However, one of their fundamental limitations results from the fault-plane/auxiliary-plane ambiguity. Applying the method described

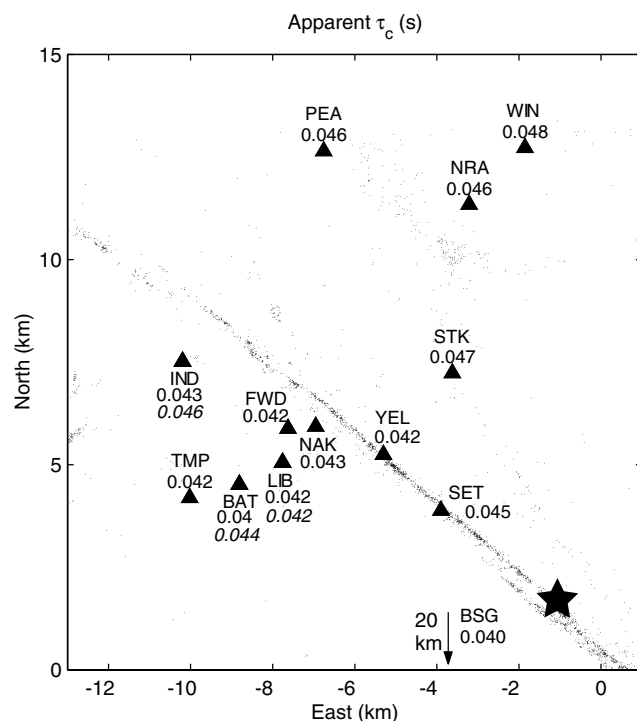


Figure 11. EGF deconvolution results for the 29 December 1994 M 2.7 earthquake. Labels are the same as Figure 9.

in this article to remove the fault-plane ambiguity from a large focal mechanism data set would be one way to increase the resolution of stress-field inversions.

Estimating Rupture Velocity

The rupture velocity of small earthquakes is an extremely important and relatively unknown quantity in earthquake physics. In particular, there is considerable interest in determining whether the rupture velocities of small earthquakes are lower than those of large earthquakes owing to the connection between rupture velocity, energy-to-moment ratio, and fault constitutive laws (Kanamori and Heaton, 2000; Guatteri and Spudich, 2000; Izutani and Kanamori, 2001; Abercrombie and Rice, 2003; Kanamori and Rivera, 2003). It has proven difficult to evaluate the dependence of radiated energy, a more commonly measured quantity, on earthquake size owing to its concentration at frequencies well above the corner frequency (Ide and Beroza, 2001). Early work supported both views, namely that small earthquake rupture velocities were significantly lower than (Bakun *et al.*, 1978) or comparable to (Frankel *et al.*, 1986) those of large earthquakes. However, many of these results were dependent on the finite rupture parameterizations imposed on the small earthquakes. More recent results by Imanishi and Takeo (2002) found low ratios of rupture to shear velocity but depended on the source model of Savage (1966) and the identification of high-frequency stopping phases that

Table 3

EGF Measurements for the 27 December 1994 Earthquake

Station	Wave Type	Measured $\mu_s^{(0,2)}$ (sec^2)	Predicted $\mu_s^{(0,2)}$ (sec^2)
SET	P	0.00050	0.00044
YEL	P	0.00045	0.00048
LIB	P	0.00044	0.00044
BAT	P	0.00039	0.00044
TMP	P	0.00045	0.00044
IND	P	0.00045	0.00046
FWD	P	0.00044	0.00045
STK	P	0.00056	0.00050
NAK	P	0.00045	0.00045
PEA	P	0.00054	0.00056
NRA	P	0.00054	0.00056
WIN	P	0.00058	0.00056
BSG	P	0.00039	0.00039
LIB	S	0.00043	0.00048
IND	S	0.00052	0.00051
BAT	S	0.00049	0.00058

The predicted values are calculated using equation (3) and the estimates of the second moments in Table 1. The difference between the third and fourth columns is the misfit in the inversion.

Table 4

EGF Measurements and Inversion Results for the 15 April 1995 Earthquake

Station	Wave Type	Measured $\mu_s^{(0,2)}$ (sec^2)	Predicted $\mu_s^{(0,2)}$ (sec^2)
UUP	P	0.00123	0.00100
IND	P	0.00092	0.00108
BAT	P	0.00106	0.00100
FWD	P	0.00103	0.00104
BRG	P	0.00163	0.00098
YEL	P	0.00088	0.00096
AKC	P	0.00101	0.00089
LIB	P	0.00100	0.00101
TMP	P	0.00073	0.00099
COW	P	0.00090	0.00093
GIB	P	0.00034	0.00051
FOR	P	0.00061	0.00065
PON	P	0.00043	0.00076
VLT	P	0.00043	0.00040
BSG	P	0.00039	0.00033
NAK	S	0.00108	0.00144
FWD	S	0.00112	0.00145
FOX	S	0.00153	0.00126
HVL	S	0.00175	0.00133
GIB	S	0.00040	0.00046

are insensitive to the termination of the rupture if it occurs gradually. The second moment estimates provide a straightforward way to examine this potential scale dependence because they are not model dependent and they are relatively insensitive to any incorrectly modeled wave propagation effects above the corner frequency.

The second moments do not uniquely determine rupture velocity in most cases owing to the effect of finite rise time

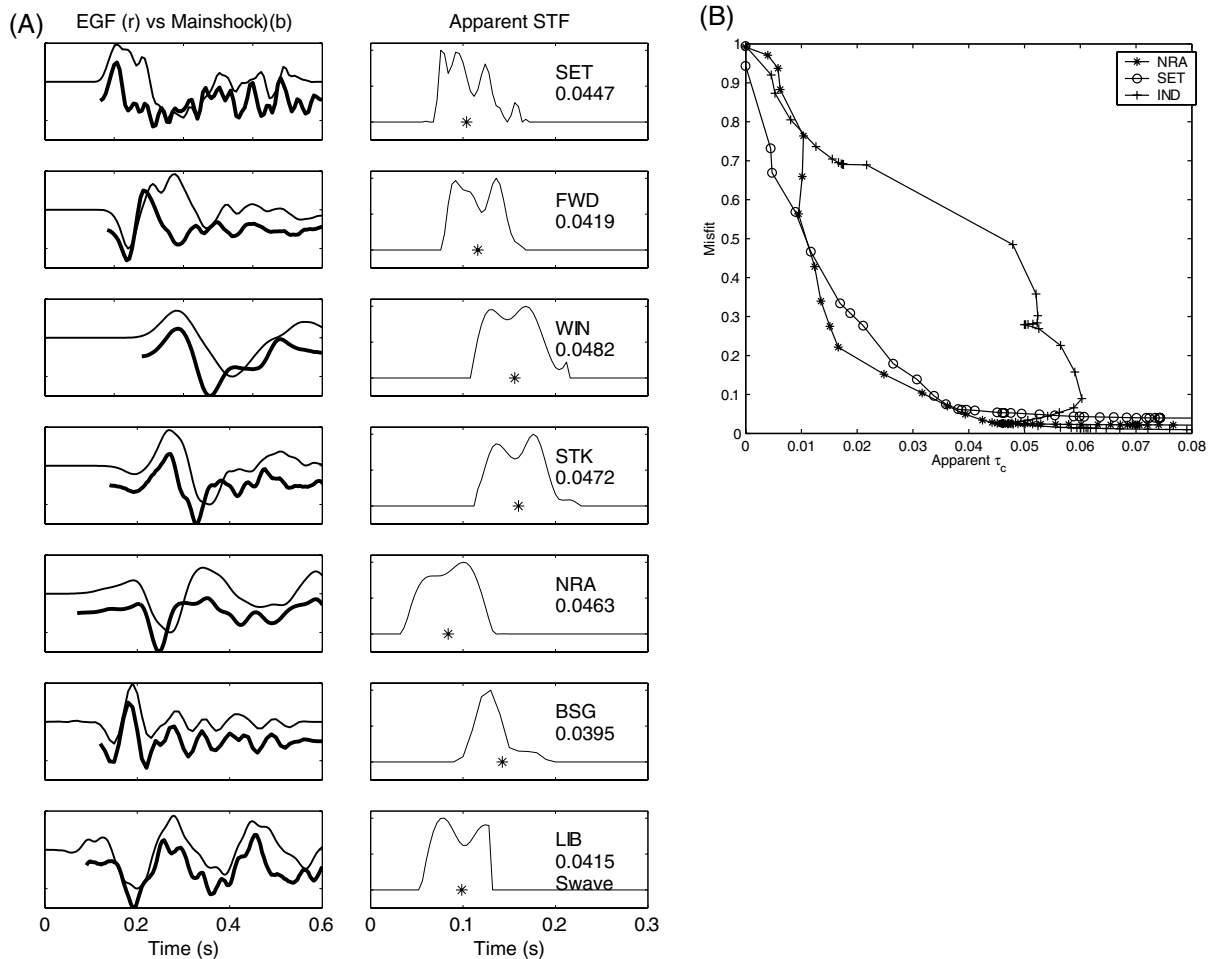


Figure 12. (A) Results of the EGF deconvolution for the 29 December 1994 M 2.7 earthquake. Labels are the same as in Figure 10. (B) Examples of the misfit versus duration trade-off for several stations similar to Figure 10. The comparison of the resulting ASTF variances (apparent τ_c) with misfit allows a visual assessment of how well constrained the apparent τ_c estimates are.

of slip at a point. Figure 15A compares values of the second moments and rupture velocity for a suite of simulated slip distributions similar to those in Figures 1 and 2. For a given value of the directivity ratio, the range of v_c/v_r values results from variation in the ratio of the rise time at a point of large slip to the total duration of the earthquake. Only for events with a directivity ratio very near 1 can useful constraints be placed on rupture velocity from estimates of the second moments. However, if there is also an estimate of the spatial offset between the epicenter and the centroid, denoted \mathbf{r}_0 , then the rupture velocity can be relatively well constrained for all events with directivity ratios above about 0.3 without reliance on any particular dynamic or simplified kinetic model. L_0 and \mathbf{r}_0 have relatively similar definitions, except that L_0 is sensitive to the duration of slip at a point (in addition to the spatial distribution of slip). Thus, the ratio of L_0 to \mathbf{r}_0 is a crude measure of the importance of finite rise time in a particular moment release distribution and can be used in combination with an estimate of v_c to constrain v_r

(Fig. 15B). Estimating \mathbf{r}_0 for small earthquakes should be a tractable problem. One approach would be to use the first-order version of equation (3):

$$\mu_s^{(0,1)} \approx \mu^{(0,1)} + s \cdot \mu^{(1,0)}, \quad (7)$$

which relates the centroid time of the ASTFs to the spatial and temporal centroids of the true slip distribution in a coordinate system with the origin at the epicenter. Thus, a similar inverse problem to the one examined in this article can be set up for the first spatial moment which defines \mathbf{r}_0 . Alternatively, waveform cross-correlation measurements are now routinely being used to locate event centroids, which may be resolveably different (by \mathbf{r}_0) from event epicenters determined with first-arrival picks.

The unilateral rupture case presented by the 1995 Bear Valley earthquake provides a relatively straightforward opportunity to evaluate the rupture velocity, v_r , of a small earth-

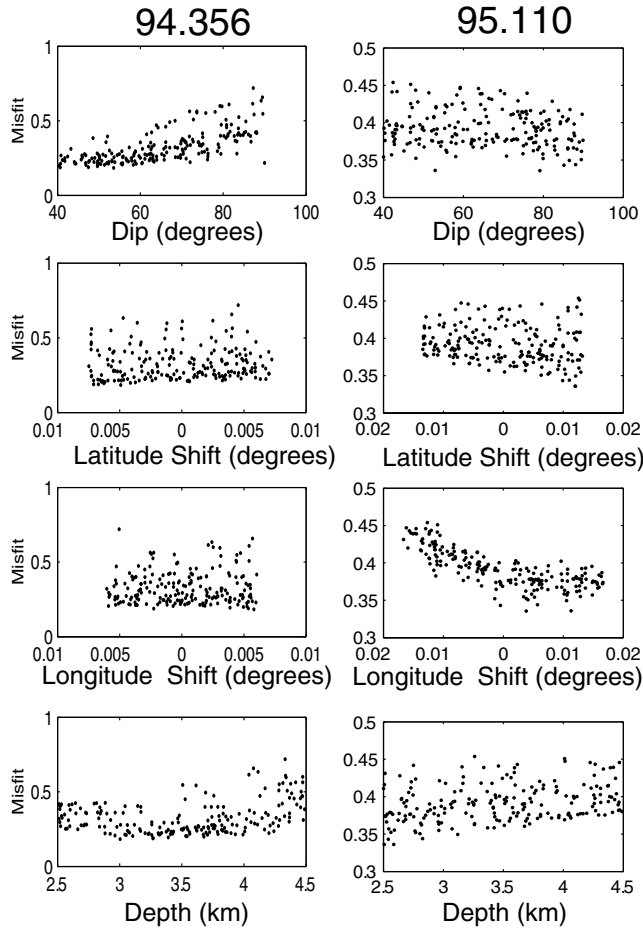


Figure 13. Comparison of the misfit of the inversion results for the 1994 and 1995 events as a function of the randomly chosen dip, latitude shift, and depth. Because the coefficient relating $\mu_s^{(0,2)}$ to $\mu^{(0,2)}$ is the same for all the measurements, the standard definition of misfit (the ratio between the sum of the squared residuals to the sum of the squared data) would appear to present extremely good fits even if the spatial variation of the $\mu_s^{(0,2)}$ values was not at all reproduced by the inversion result. Instead, we defined misfit as the ratio between the sum of the squared residuals and the sum of the squared difference between the data and the mean of the data. This definition of misfit ranges from a value of 1 if only the average value of the data are reproduced by the inversion to a value of 0 if the spatial variation of the data is exactly reproduced by the inversion.

quake owing to its high directivity ratio. Thus, the propagation velocity of the rupture front in the 1995 event was likely in the 2.0- to 2.2-km/sec range. For a mode two rupture (propagation parallel to the slip direction), like the 1995 event, the typical upper limit to the v_r is the Rayleigh speed, c_R (0.92 of the shear-wave speed [Scholz, 1990]). The P -wave velocity at the source depth is approximately 5.25 and 4.75 km/sec on the southwest and northeast sides of the fault, respectively (Thurber *et al.*, 1997). The v_p/v_s ratio is poten-

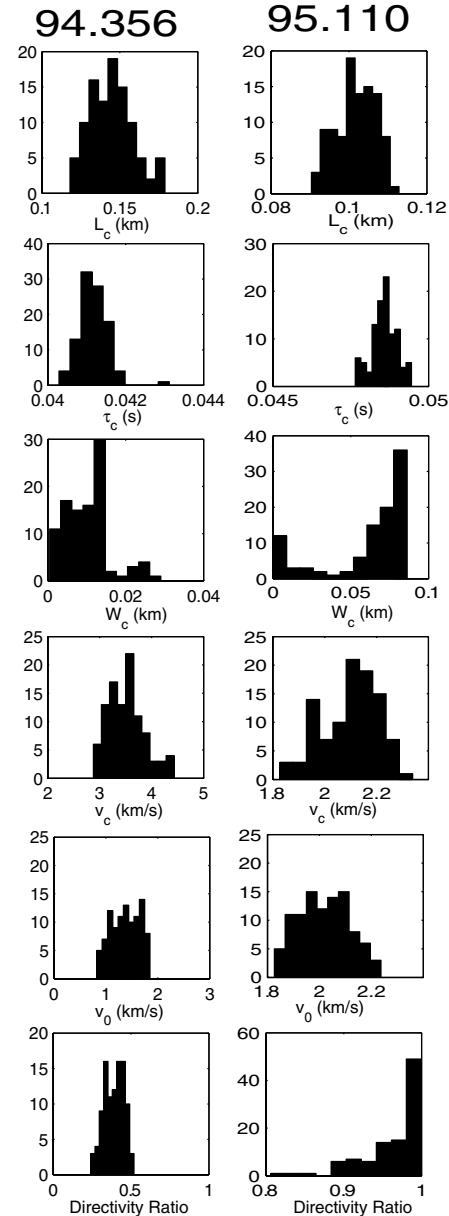


Figure 14. Histograms showing the distribution of the various characteristic quantities that describe the rupture for inversion runs with low misfit values. The y axes of the histograms give the percentage of inversion results within a particular x-axis bin. For the 1995 event, the fault dip was constrained between 60° and 80°, the latitude and longitude shifts between 0° and 0.01°, and the depth between 2 and 4 km. For the 1994 event, the fault dip was constrained between 60° and 80°, the latitude and longitude shifts between $\pm 0.005^\circ$, and the depth between 3 and 4 km.

tially high in the actual fault zone material, probably ranging from about 1.7 to 2.0 (Thurber *et al.*, 1997). The material property contrast across the fault and the variability in Poisson's ratio lead to a range of potential shear-wave speeds between about 2.4 and 3.0 km/sec. Thus, the lower bound

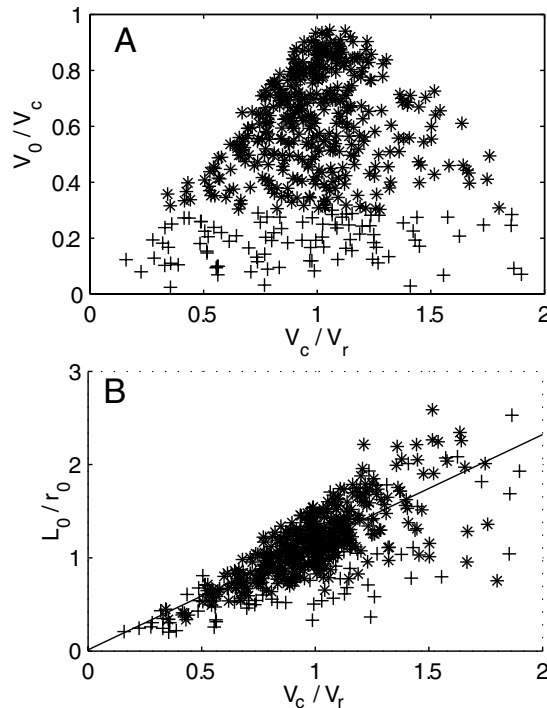


Figure 15. (A) Comparison of second moment values and rupture velocity (i.e., the propagation velocity of the rupture front) for a suite of randomly generated simulations similar to those in Figures 1 and 2. Events with a directivity ratio above and below 0.3 are plotted with asterisk and plus marks, respectively. For a particular value of the directivity ratio (y axis), the range of v_c/v_r values is a result of variation in the finite rise time at a point. In particular, events with low v_c/v_r correspond to ones where the rise time at a point was relatively long, and the large values correspond to simulations where the rise time was relatively fast. In the limit of instantaneous rise time, the simulations lie on the line from (1,1) to (2,0). When only the second moments are known, the rupture velocity can not be usefully constrained unless the directivity ratio is very near 1. (B) The same simulations as panel A, but with the distance between the epicenter and the centroid, r_0 , utilized in the ordinate. If an estimate of r_0 is combined with estimates of the second moments, the uncertainty in rupture velocity that results from finite rise time effects is greatly reduced, at least for ruptures with a directivity ratio larger than about 0.3.

on the ratio v_r/c_R is about 0.76 [2.1 km/sec/(0.92 * 3.0) km/sec] with values in the 0.8–0.85 range being likely. These values lie in the range typically quoted for large earthquakes such as Landers ($v_0 = 2.2$ km/sec; McGuire *et al.*, 2002). While this result is only for one earthquake, it demonstrates that evaluating the scaling of rupture velocity and other quantities derived from the second moments is an approach that can address fundamental questions without a dependence on any assumed source model.

Acknowledgments

I would like to thank Cezar Trifu, Michael Pasyanos, and an anonymous reviewer for helpful comments. This research was partially supported by the Southern California Earthquake Center. SCEC is funded by NSF Cooperative Agreement EAR-0106924 and USGS Cooperative Agreement 02HQA0008. The SCEC contribution number for this article is 745. This work was also supported by the Andrew W. Mellon Foundation Endowed Fund for Innovative Research.

References

- Abercrombie, R. E., and J. Rice (2003). Can observations of earthquake scaling constrain slip weakening? *Geophys. J. Int.* (in press).
- Aki, K. (1967). Scaling law of seismic spectrum, *J. Geophys. Res.* **72**, 1217–1231.
- Backus, G., and M. Mulcahy (1976a). Moment tensors and other phenomenological descriptions of seismic sources I. Continuous displacements, *Geophys. J. R. Astr. Soc.* **46**, 341–361.
- Backus, G., and M. Mulcahy (1976b). Moment tensors and other phenomenological descriptions of seismic sources II. Discontinuous displacements, *Geophys. J. R. Astr. Soc.* **47**, 301–329.
- Backus, G. E. (1977a). Interpreting the seismic glut moments of total degree two or less, *Geophys. J. R. Astr. Soc.* **51**, 1–25.
- Backus, G. E. (1977b). Seismic sources with observable glut moments of spatial degree two, *Geophys. J. R. Astr. Soc.* **51**, 27–45.
- Bakun, W. H., R. M. Stewart, C. G. Bufe (1978). Directivity in the high-frequency radiation of small earthquakes, *Bull. Seism. Soc. Am.* **68**, 1253–1263.
- Ben-Menahem, A. (1961). Radiation of seismic waves from finite moving sources, *Bull. Seism. Soc. Am.* **51**, 403–435.
- Betero, M., D. Bindi, P. Boccacci, M. Cattaneo, C. Eva, and V. Lanza (1997). Application of the project Landweber method to the estimation of the source time function in seismology, *Inverse Theory* **13**, 458–486.
- Boatwright, J. (1980). A spectral theory for circular seismic sources: simple estimates of source dimension, dynamic stress drop, and radiated energy, *Bull. Seism. Soc. Am.* **70**, 1–28.
- Brune, J. N. (1970). Tectonic stress and the seismic shear waves from earthquakes, *J. Geophys. Res.* **75**, 4997–5009.
- Doornbos, D. J. (1982). Seismic source spectra and moment tensors, *Phys. Earth Planet. Int.* **30**, 214–227.
- Dreger, D. S. (1994). Empirical Green's function study of the January 17, 1994 Northridge California earthquake, *Geophys. Res. Lett.* **21**, 2633–2636.
- Eshelby, J. D. (1957). The determination of the elastic field of an ellipsoidal inclusion and related problems, *Proc. R. Soc. London* **241**, 376–396.
- Frankel, A., and H. Kanamori (1983). Determination of rupture duration and stress drop for earthquakes in southern California, *Bull. Seism. Soc. Am.* **73**, 1527–1551.
- Frankel, A., J. B. Fletcher, F. Vernon, L. C. Haar, J. Berger, T. C. Hanks, and J. N. Brune (1986). Rupture characteristics and tomographic source imaging of M_L approximately 3 earthquakes near Anza, southern California, *J. Geophys. Res.* **91**, 12,633–12,650.
- Guatteri, M., and P. Spudich (2000). What can strong motion data tell us about slip-weakening fault friction laws? *Bull. Seism. Soc. Am.* **90**, 98–116.
- Hardebeck, J. L., and E. Hauksson (2001). Crustal stress field in southern California and implications for fault mechanics, *J. Geophys. Res.* **106**, 21,859–21,882.
- Hartzell, S. H. (1978). Earthquake aftershocks as Green's functions, *Geophys. Res. Lett.* **5**, 1–4.
- Ide, S. (2001). Complex source processes and the interaction of moderate earthquakes during the earthquake swarm in the Hida-Mountains, Japan, *Tectonophysics* **334**, 35–54.

- Ide, S., and G. Beroza (2001). Does apparent stress vary with earthquake size? *Geophys. Res. Lett.* **28**, 3349–3352.
- Imanishi, K., and M. Takeo (2002). An inversion method to analyze rupture processes of small earthquakes using stopping phases, *J. Geophys. Res.* **107**, doi 10.1029/2001JB000201.
- Izutani, Y., and H. Kanamori (2001). Scale-dependence of seismic energy to moment ratio for strike slip earthquakes in Japan, *Geophys. Res. Lett.* **28**, 4007–4010.
- Kanamori, H., and T. H. Heaton (2000). Microscopic and macroscopic physics of earthquakes, in *Physics of Earthquakes*, Vol. 1, AGU, 147–163.
- Kanamori, H., and L. Rivera (2004). Static and dynamic scaling relations for earthquakes and their implications for rupture speed and stress drop, *Bull. Seism. Soc. Am.* **94**, no. 1, 314–319.
- Lanza, V., D. Spallarossa, M. Cattaneo, D. Bindi, and P. Augliera (1999). Source parameters of small events using constrained deconvolution with empirical Green's functions, *Geophys. J. Int.* **137**, 651–652.
- Madariaga, R. (1976). Dynamics of an expanding circular fault, *Bull. Seism. Soc. Am.* **66**, 639–666.
- McGuire, J. J., L. Zhao, and T. H. Jordan (2001). Measuring the second-degree moments of earthquake space-time distributions, *Geophys. J. Int.* **145**, 661–678.
- McGuire, J. J., L. Zhao, and T. H. Jordan (2002). Predominance of unilateral rupture for a global catalog of large earthquakes, *Bull. Seism. Soc. Am.* **92**, no. 8, 3309–3317.
- McNally, K. C., and T. V. McEvilly (1977). Velocity contrast across the San Andreas fault in central California: small-scale variations from *P*-wave nodal plane distortion, *Bull. Seism. Soc. Am.* **67**, 1565–1576.
- Rubin, A. M. (2002). Aftershocks of microearthquakes as probes of the mechanics of rupture, *J. Geophys. Res.* **107**, doi 10.1029/2001JB000496.
- Rubin, A. M., and D. Gillard (2000). Aftershock asymmetry/rupture directivity among central San Andreas fault microearthquakes, *J. Geophys. Res.* **105**, 19,095–19,109.
- Savage, J. C. (1966). Radiation from a realistic model of faulting, *Bull. Seism. Soc. Am.* **56**, 577–592.
- Scholz, C. H. (1990). *The Mechanics of Earthquake Faulting*, Cambridge U Press, New York.
- Silver, P. (1983). Retrieval of source-extent parameters and the interpretation of corner frequency, *Bull. Seism. Soc. Am.* **73**, 1499–1511.
- Silver, P. G., and T. H. Jordan (1983). Total-moment spectra of fourteen large earthquakes, *J. Geophys. Res.* **88**, 3273–3293.
- Stewart, S. W. (1968). Preliminary comparison of seismic traveltimes and inferred crustal structure adjacent to the San Andreas fault in the Diablo and Gabilan ranges of central California, Stanford University Publications, Geological Sciences, Vol. 11, 218–230.
- Thurber, C., S. Roecker, W. Ellsworth, Y. Chen, W. Lutter, and R. Sessions (1997). Two-dimensional seismic image of the San Andreas fault in the Northern Gabilan Range, central California: evidence for fluids in the fault zone, *Geophys. Res. Lett.* **24**, 1591–1594.
- Vandenberghe, L., and S. Boyd (1996). Semidefinite programming, *SIAM Rev.* **38**, 49–95.
- Venkataraman, A., J. Mori, H. Kanamori, and L. Zhu (2000). Fine structure of the rupture zone of the April 26 and 27, 1997, Northridge aftershocks, *J. Geophys. Res.* **105**, 19,085–19,093.
- Wald, D. J., and T. H. Heaton (1994). Spatial and temporal distribution of slip for the 1992 Landers, California, earthquake, *Bull. Seism. Soc. Am.* **84**, 668–691.
- Wald, D. J., D. Helmberger, and T. H. Heaton (1991). Rupture model of the 1989 Loma Prieta earthquake from the inversion of strong ground motion and broadband teleseismic teleseismic data, *Bull. Seism. Soc. Am.* **81**, 1540–1572.
- Waldhauser, F., and W. Ellsworth (2000). A double-difference earthquake location algorithm: method and application to the northern Hayward fault, *Bull. Seism. Soc. Am.* **90**, 1330–1368.
- Walter, A. W., and W. D. Mooney (1982). Crustal structure of the Diablo and Gabilan ranges central California: a reinterpretation of existing data, *Bull. Seism. Soc. Am.* **72**, 1567–1590.

Department of Geology and Geophysics
Woods Hole Oceanographic Institution
Woods Hole, Massachusetts 02543

Manuscript received 12 May 2003.